IOP Publishing Smart Materials and Structures
Smart Mater. Struct. **22** (2013) 045010 (12pp) doi:10.1088/0964-1726/22/4/045010

Underwater tracking of a moving dipole source using an artificial lateral line: algorithm and experimental validation with ionic polymer–metal composite flow sensors

Ahmad T Abdulsadda[1,2] **and Xiaobo Tan**[2]

[1] Communication Department, Al Najaf Technical College, Abo Skeer Street, Al Najaf, Iraq
[2] Smart Microsystems Laboratory, Department of Electrical and Computer Engineering, Michigan State University, East Lansing, MI 48824, USA

E-mail: abdulsad@msu.edu and xbtan@msu.edu

Received 22 October 2012, in final form 7 January 2013
Published 7 March 2013
Online at stacks.iop.org/SMS/22/045010

Abstract
Motivated by the lateral line system of fish, arrays of flow sensors have been proposed as a new sensing modality for underwater robots. Existing studies on such artificial lateral lines (ALLs) have been mostly focused on the localization of a fixed underwater vibrating sphere (dipole source). In this paper we examine the problem of tracking a moving dipole source using an ALL system. Based on an analytical model for the moving dipole-generated flow field, we formulate a nonlinear estimation problem that aims to minimize the error between the measured and model-predicted magnitudes of flow velocities at the sensor sites, which is subsequently solved with the Gauss–Newton scheme. A sliding discrete Fourier transform (SDFT) algorithm is proposed to efficiently compute the evolving signal magnitudes based on the flow velocity measurements. Simulation indicates that it is adequate and more computationally efficient to use only the signal magnitudes corresponding to the dipole vibration frequency. Finally, experiments conducted with an artificial lateral line consisting of six ionic polymer–metal composite (IPMC) flow sensors demonstrate that the proposed scheme is able to simultaneously locate the moving dipole and estimate its vibration amplitude and traveling speed with small errors.

(Some figures may appear in colour only in the online journal)

1. Introduction

Fish and amphibians rely on the lateral line system to obtain flow information of interest [1, 2]. A lateral line comprises arrays of mechanoreceptive units called neuromasts, each of which consists of a bundle of sensory hair cells encapsulated in a gelatinous cupula [3]. Neuromasts can be found standing external to the skin (superficial neuromasts) and in fluid-filled canals below the skin surface (canal neuromasts), which tend to respond to flow velocities and flow accelerations, respectively, around the animal's body [4, 5]. It has been demonstrated that the lateral line plays a pronounced role in predator detection and prey capture [6, 7], object detection and avoidance [8, 9], rheotaxis [10] and energy-efficient swimming [11] among other behaviors.

The lateral line system has inspired a number of efforts to create an engineering equivalent to facilitate the navigation, coordination and control of underwater robots and vehicles [2, 12]. Over the last decade, several research groups have reported microfabricated flow sensors that to varying degrees

have been motivated by fish neuromasts [13–16] or the wind receptor hairs of insects [17, 18]. Hair cell-inspired sensors have also been developed at milli- to centimeter scales, and are based on optical transduction [19] or novel sensing materials such as ionic polymer–metal composites (IPMCs) [20, 21] and gel-supported lipid bilayers [22].

On the signal processing aspect for artificial lateral lines (ALLs), while there has been experimental work in exploring the strategies for vortex sensing [19, 23, 24] and object tracking and recognition [25], most relevant work has been focused on the localization of a vibrating sphere, known as a dipole source. A dipole source can emulate the rhythmic movement of fins and body appendages, and has been widely used as a stimulus (playing the role of predator, prey or conspecific) in the study of biological lateral lines [26, 27]. Dipole source localization has also become a benchmark problem in the development of ALLs, for demonstration of the latter's capability to mimic their biological counterpart [16, 21, 28–30]. In addition, for underwater applications, localization of dipole sources has implications for the detection estimation of nearby fish-like robots and therefore is relevant to robot coordination and control. Various strategies for dipole source localization have been proposed. For example, Dagamseh *et al* proposed localization based on the characteristic points (zero-crossings, maxima, etc) in the measured velocity profile along the lateral line [29]. Franosch *et al* suggested a maximum-likelihood estimator-type model for dipole localization by *Xenopus* [31], which is relevant to the engineering setting. Data-matching/table-lookup approaches were presented by Pandya *et al*, where the measured signal pattern was compared with a large, pre-obtained set of templates or an empirical model fitted with a sufficient number of data [28]. A beamforming algorithm for array signal processing was used to localize a dipole source and a tail-flicking crayfish by Yang *et al* [30]. In previous works we proposed a neural network-based scheme [21] and a nonlinear estimation method [32] for dipole localization.

Despite the aforementioned extensive work on dipole source localization, existing studies have been predominantly limited to the case of a *fixed* dipole. In this paper we present, to our best knowledge, the first studies on localizing a *moving* dipole source using an ALL. Such a moving source could represent a swimming or robotic fish, which naturally demonstrate a combination of translational motion and oscillatory body/fin motion. First, we formulate a nonlinear estimation problem based on an analytical model for the moving dipole-generated flow field, where we assume that the source location, vibration amplitude and speed of movement are unknown, and aim to minimize the error between the measured and model-predicted magnitudes of flow velocities at the sensor sites. In particular, since the flow velocities contain both a DC component and an AC component that corresponds to the frequency of dipole vibration, the cost function for minimization consists of a convex combination of terms associated with the DC and AC components, respectively. The minimization problem is solved recursively with the Gauss–Newton scheme. A sliding discrete Fourier transform (SDFT) algorithm is proposed to efficiently compute the evolving signal magnitudes at the DC and AC frequencies based on the flow velocity measurements. Simulation is conducted to assess the performance of the proposed scheme, and we find that it is adequate to consider only the AC component of the flow velocities in the estimation; namely, the DC component can be excluded from the cost function to minimize. The latter scheme is more computationally efficient than a scheme involving both the DC and AC components, due to the savings in both the SDFT evaluation and in the Gauss–Newton iteration. In addition, since in practice it is often difficult to obtain precise measurement of the DC component (as we discuss later), the latter finding justifies the use of the AC component only in experimental validation.

We have validated the proposed algorithm experimentally with an ALL prototype comprising an array of IPMC sensors. IPMCs are a class of soft sensing and actuation materials that have received significant interest over the past two decades [33–44]. An IPMC has three layers, with an ion-exchange polymer membrane sandwiched by metal electrodes. Inside the polymer, anions covalently fixed to polymer chains are balanced by mobile cations. The sensing mechanism of an IPMC can be explained as follows. When the IPMC is deformed under a mechanical stimulus (e.g. force, pressure and flow), the cations inside will redistribute, which results in a detectable electric signal (e.g. short-circuit current) [45]. On the other hand, when an voltage is applied across an IPMC, the electric field will drive the transport of hydrated cations and water molecules within the membrane; this, together with the associated electrostatic interactions, will cause the bending of the IPMC, which explains the actuation mechanism of the material [33, 45]. Recent years have seen significant interest in the fabrication [36, 39, 46], characterization and modeling [33, 38, 42, 47–52] of IPMC sensors and actuators. A number of groups have explored IPMC materials for underwater actuation [40, 41, 53–57], sensing [58] and energy harvesting [43]. In particular, our previous work has demonstrated the feasibility of IPMC sensors in flow sensing [21, 59]. In this work, with an artificial line consisting of six IPMC sensors, each being 8 mm long, 2 mm wide and 200 μm thick, we show that the proposed method is capable of simultaneously locating the moving dipole and estimating its vibration amplitude and traveling speed with small errors.

The remainder of the paper is organized as follows. The localization algorithm, including the problem formulation, the Gauss–Newton scheme and the SDFT scheme, is presented in section 2. Simulation and experimental results are presented in sections 3 and 4, respectively. Finally, concluding remarks are provided in section 5.

2. Algorithm for the localization of a traveling dipole source

2.1. Problem setup

Figure 1 illustrates the problem setup considered in this paper, where a dipole source is vibrating and traveling in the

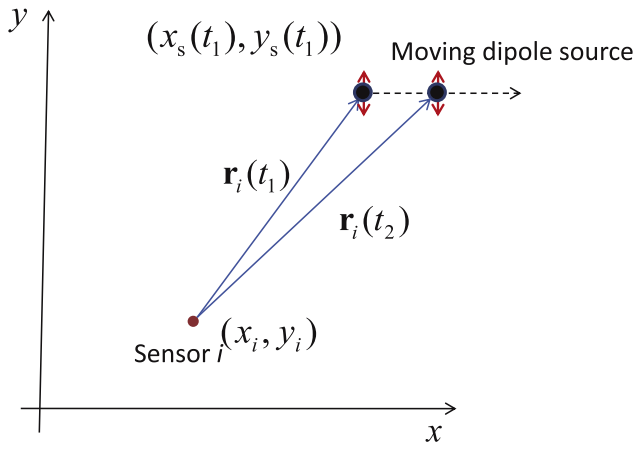

Figure 1. Illustration of the problem setup for the localization of a traveling dipole source.

two-dimensional x–y plane. An ALL comprising N sensors is located in parallel to the x-axis, with the sensor locations denoted as (x_i, y_i), $0 \le i \le N-1$. We denote the location of a dipole source at time t by $(x_s(t), y_s(t))$. For ease of presentation, we assume that the vibration axis of the source is parallel to the y-axis, with the corresponding vibration velocity denoted as $v_1(t) = \omega A \sin(\omega t + \phi)$, where A and ω are the vibration amplitude and angular frequency, respectively. We further assume that the source is traveling along the x-direction with a constant speed of v_0.

Since most existing flow sensors are only able to measure the flow velocity in one direction, without loss of generality, we will assume that each sensor can provide a noisy measurement of v_x, the x-component of the local flow velocity. The approach proposed in this work can be extended with ease to cases where the lateral line sensors measure v_y, the y-component of the flow velocities, or cases where some sensors measure v_x while others measure v_y. Under an assumption of ideal flows, v_x at the site of sensor i can be derived as [60]

$$\begin{aligned} v_x(x_i, y_i, t) = \{a^3[(2(x_i - x_s(t))^2 - (y_i - y_s(t))^2)v_0 \\ + 3(x_i - x_s(t))(y_i - y_s(t))v_1(t)]\} \\ \times \{2\|\mathbf{r}_i(t)\|^5\}^{-1}, \end{aligned} \tag{1}$$

where $\mathbf{r}_i(t) = (x_s(t) - x_i, y_s(t) - y_i)^T$, with the superscript T denoting the transpose, and a represents the radius of the sphere.

The localization and tracking problem is defined as follows. Assume that the sphere diameter a and vibration frequency ω are known but the vibration velocity amplitude A and phase ϕ and the source traveling speed v_0 are unknown. Given the measurements of $v_x(x_i, y_i, \tau)$, $0 \le \tau \le t$, $0 \le i \le N-1$, provide an estimate of the current source location $(x_s(t), y_s(t))$.

2.2. Tracking approach

From (1), the local flow velocity generated by the moving dipole has two terms, one corresponding to the translation motion and the other corresponding to the vibration. When the change of source location $(x_s(t), y_s(t))$ is relatively slow with respect to the dipole vibration $v_1(t)$, the frequency spectrum of the signal $v_x(x_i, y_i, \cdot)$ will consist primarily of two components at DC and ω, respectively. Our proposed approach involves computing the magnitudes of these two frequency components, denoted as $m_{0,i}$ and $m_{1,i}$, based on the signal $v_x(x_i, y_i, \cdot)$, and then using the obtained $\{m_{0,i}, m_{1,i}\}_{i=0}^{N-1}$ to estimate the source location and other parameters of interest. A major advantage of this approach is its robustness to measurement noises—the inherent filtering effect of computing $m_{0,i}$ and $m_{1,i}$ allows us to remove noises at all other frequencies.

We will discuss how the empirical values of $m_{0,i}$ and $m_{1,i}$ are obtained in section 2.3; in this subsection we focus on parameter estimation assuming that the measurements of $m_{0,i}$ and $m_{1,i}$ are available. Clearly, the magnitudes $\{m_{0,i}, m_{1,i}\}$ are time dependent due to the time-varying nature of (x_s, y_s); for simplicity of notation, the latter dependence is kept implicit in the following discussion. For a quasi-static source location (x_s, y_s), we derive from (1)

$$m_{0,i} = f_{0,i}(\theta) \triangleq \left| \frac{a^3}{2\|\mathbf{r}_i\|^5}(2(x_i - x_s)^2 - (y_i - y_s)^2)v_0 \right|, \tag{2}$$

$$m_{1,i} = f_{1,i}(\theta) \triangleq \left| \frac{a^3\omega}{2\|\mathbf{r}_i\|^5}(3(x_i - x_s)(y_i - y_s)A) \right|, \tag{3}$$

where $\theta = (v_0, A, x_s, y_s)$ represents the set of parameters of interest.

We further define

$$\begin{aligned} m_0 &\triangleq (m_{0,0}, \ldots, m_{0,N-1})^T, \\ m_1 &\triangleq (m_{1,0}, \ldots, m_{1,N-1})^T, \\ f_0(\theta) &\triangleq (f_{0,0}(\theta), \ldots, f_{0,N-1}(\theta))^T, \\ f_1(\theta) &\triangleq (f_{1,0}(\theta), \ldots, f_{1,N-1}(\theta))^T. \end{aligned}$$

Let $\hat{m}_0$ and $\hat{m}_1$ denote the magnitudes of the DC and AC (frequency ω) components, respectively, evaluated from the measured signals $\{v_x(x_i, y_i, \cdot)\}_{i=0}^{N-1}$. We would like to obtain an estimate of the parameter vector, $\hat{\theta}(t) = (\hat{v}_m, \hat{A}, \hat{x}_s(t), \hat{y}_s(t))$, such that a cost function

$$\begin{aligned} J(\hat{\theta}) = \beta(\hat{m}_0 - f_0(\hat{\theta}))^T(\hat{m}_0 - f_0(\hat{\theta})) \\ + (1 - \beta)(\hat{m}_1 - f_1(\hat{\theta}))^T(\hat{m}_1 - f_1(\hat{\theta})) \end{aligned} \tag{4}$$

is minimized, where $\beta \in [0, 1]$ is a parameter weighting the importance of the DC term relative to the oscillatory terms.

While $f_0(\theta)$ and $f_1(\theta)$ are linear in v_0 and A, they are highly nonlinear in (x_s, y_s). The problem of minimizing J in (4) is thus similar to the problem of localizing a stationary dipole source as formulated in our previous work [32], where two iterative schemes were proposed to solve the nonlinear estimation problem. The first scheme, which is based on the Gauss–Newton method, involves iterative linearization of the nonlinear functions, as we explain below. In the second scheme, the Newton–Raphson method is used to solve the nonlinear equation resulting from the first-order optimality condition. Overall the two schemes were shown to have

comparable performance with Gauss–Newton having a slight advantage [32]. Therefore, we will adopt the Gauss–Newton scheme in this paper. First we approximate f_0 and f_1 by linearizing them around some nominal point $\bar{\theta}$:

$$\bar{f}_0(\theta) = f_0(\bar{\theta}) + B_0(\bar{\theta})(\theta - \bar{\theta}),$$
$$\bar{f}_1(\theta) = f_1(\bar{\theta}) + B_1(\bar{\theta})(\theta - \bar{\theta}),$$

where

$$B_0(\bar{\theta}) = \left.\frac{\partial f_0}{\partial \theta}\right|_{\theta=\bar{\theta}}, \qquad B_1(\bar{\theta}) = \left.\frac{\partial f_1}{\partial \theta}\right|_{\theta=\bar{\theta}}.$$

Accordingly, we modify the cost function for the estimation problem from (4) to

$$J_1(\hat{\theta}) = \beta(\hat{m}_0 - \bar{f}_0(\hat{\theta}))^{\mathrm{T}}(\hat{m}_0 - \bar{f}_0(\hat{\theta})) + (1-\beta)(\hat{m}_1 - \bar{f}_1(\hat{\theta}))^{\mathrm{T}}(\hat{m}_1 - \bar{f}_1(\hat{\theta})). \quad (5)$$

Finding the minimizing $\hat{\theta}$ for J_1 is a standard least-squares optimization problem, a solution of which is given by

$$\hat{\theta} = \bar{\theta} + \lambda(\beta B_0(\bar{\theta})^{\mathrm{T}} B_0(\bar{\theta}) + (1-\beta) B_1(\bar{\theta})^{\mathrm{T}} B_1(\bar{\theta}))^{-1} \times (\beta B_0^{\mathrm{T}}(\bar{\theta})(\hat{m}_0 - f_0(\bar{\theta})) + (1-\beta) B_1^{\mathrm{T}}(\bar{\theta})(\hat{m}_1 - f_1(\bar{\theta}))), \quad (6)$$

where $\lambda > 0$ is a stepping parameter. In implementation a recursive version of (6) is adopted to update the estimate, to mitigate the impact introduced by linearization:

$$\hat{\theta}_{k+1} = \hat{\theta}_k + \lambda(\beta B_0(\hat{\theta}_k)^{\mathrm{T}} B_0(\hat{\theta}_k) + (1-\beta) B_1(\hat{\theta}_k)^{\mathrm{T}} B_1(\hat{\theta}_k))^{-1} \times (\beta B_0^{\mathrm{T}}(\hat{\theta}_k)(\hat{m}_0 - f_0(\hat{\theta}_k)) + (1-\beta) B_1^{\mathrm{T}}(\hat{\theta}_k)(\hat{m}_1 - f_1(\hat{\theta}_k))), \quad (7)$$

where the initial estimate $\hat{\theta}_0$ is chosen properly. The iteration is stopped when $\|\hat{\theta}_{k+1} - \hat{\theta}_k\| \leq \epsilon$, where $\epsilon > 0$ is a specified tolerance and $\|\cdot\|$ denotes the Euclidean norm of a vector.

Note that in (7), $B_0(\hat{\theta}_k)$ and $B_1(\hat{\theta}_k)$ have dimensions of $N \times D_\theta$, where $D_\theta = 4$ denotes the dimension of the vector θ. Consequently, the inverted matrix in (7) has dimensions of $D_\theta \times D_\theta$. Therefore, the complexity of matrix inversion, the most computationally expensive operation in the algorithm, does not grow with the number N of sensors.

2.3. The sliding discrete Fourier transform (SDFT) algorithm

Since the actual sensor output is a discrete-time signal, discrete Fourier transform (DFT) could be used to extract the signal amplitudes at different frequencies. However, because the dipole source is moving, the amplitudes m_0 and m_1 evolve with the time index n and it is thus not practical to collect a large sequence of sensor data and perform DFT to extract the measurements $\hat{m}_0$ and $\hat{m}_1$. The SDFT algorithm [61, 62] is particularly suitable for computing a specific spectral bin in real-time application based on a sliding window of time samples. For this reason, it has been adopted to compute the two frequency components of interest in this paper.

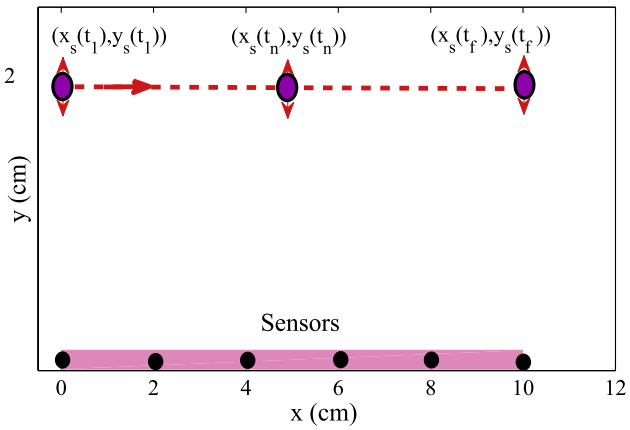

Figure 2. Illustration of the simulation setup.

For a window of M time samples collected by the ith sensor, rewritten as $\{v_i[n-(M-1)], \ldots, v_i[n]\}$, we can evaluate the pth spectral bin using DFT:

$$V_{p,i}[n] = \sum_{k=0}^{M-1} v_i[n-M+1+k]\mathrm{e}^{-\mathrm{j}2\pi pk/M}, \quad \text{for } 0 \leq p \leq M-1. \quad (8)$$

As discussed in section 2.2, there are two frequencies that are of interest to us, the DC signal (spectral bin $p = 0$) and the signal with angular frequency ω (spectral bin $p = \left[\frac{\omega M}{2\pi F_s}\right]$), where $[\cdot]$ denotes rounding to the nearest integer and F_s is the sampling frequency to obtain sensors signals $v_i[\cdot]$. Exploiting the fact that all elements but one in neighboring windows are identical, we can efficiently evaluate $V_{p,i}[n]$ recursively with the SDFT algorithm:

$$V_{p,i}[n] = \mathrm{e}^{-\mathrm{j}\omega_0}(V_{p,i}[n-1] - v_i[n-M] + v_i[n]), \quad (9)$$

where $\omega_o = 2\pi p/M$.

For $p = 0$, from (8) we can see that $V_{0,i}[n]$ essentially sums up the M signal samples in the window. Consequently, the magnitude $\hat{m}_{0,i}$ of the DC component for $\{v_i[\cdot]\}$ is $\frac{|V_{0,i}[n]|}{M}$. For the AC component $\left(p = \left[\frac{\omega M}{2\pi F_s}\right]\right)$, one can readily derive its magnitude $\hat{m}_{1,i}$ as $\frac{|2V_{p,i}[n]|}{M}$.

3. Simulation results

Figure 2 illustrates the simulation setup. The setup and the simulation parameters are largely based on the real experimental conditions (see section 4). The lateral line system is placed parallel to the x-axis and centered at (0, 5) cm. It consists of six sensors, with a sensor-to-sensor separation of 2 cm. The dipole vibration frequency is set to be 40 Hz, which is consistent with the typical range of dipole frequencies adopted in the study of biological and artificial lateral lines (e.g. 50 Hz in [63] and 45 Hz in [30, 64]). The dipole size a and vibration amplitude A are assumed to be 1.9 cm and 0.191 cm, respectively. The dipole is assumed to travel at a constant speed of $v_0 = 1.5$ cm s^{-1} from left

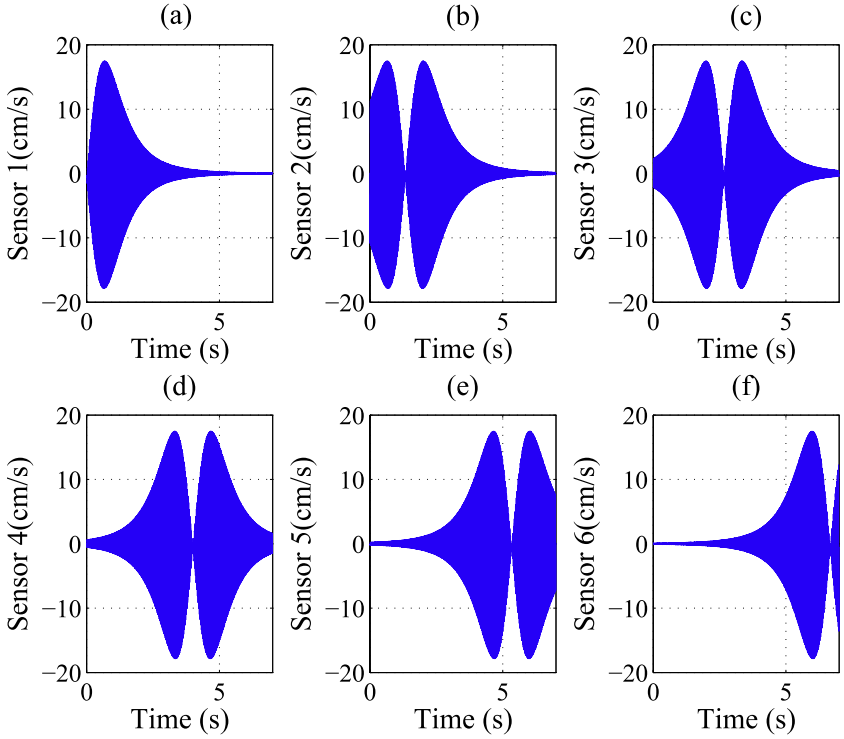

Figure 3. Simulation results: time trajectories of the flow velocities at the sensor locations.

to right. The choice of this speed is partly motivated by the constraint in our experimental setup, but it is also within the typical speed range of small robotic fish [65]. The impact of v_0 will be further discussed in section 5.

Figure 3 shows the simulated flow velocities (x-component) at each sensor site, where the initial location of the dipole source is (0, 2) cm. Based on the measured noise level of our IPMC flow sensors in the experimental prototype, we consider an additive Gaussian noise with zero mean and variance of 0.0065 cm^2 s^{-2} for each sensor.

Figures 4 and 5 show the magnitudes of the DC and AC components, respectively, obtained through SDFT. The sampling frequency used is 20 kHz, and the sliding window size is 500 samples (25 ms). Within each window, the dipole travels 0.375 mm and the resulting flow velocity at each sensor site is nearly constant. It is clear from figures 4 and 5 that both the DC and AC components contain relevant information for localizing the source, as can be seen from the shifting magnitude profiles in the figures.

Using the computed DC and AC magnitudes, we have conducted the tracking of the dipole source with the Gauss–Newton algorithm described in section 2.2. In order to explore the influence of the weighting parameter β on the tracking performance, we have tried two different values of β, 0.5 and 0. When $\beta = 0.5$, equal weights are placed on the DC and AC components, while when $\beta = 0$, we rely only on the AC component for localization. While the SDFT is used to update $\hat{m}_0$ and $\hat{m}_1$ at each sampling time, the estimation is only conducted every 0.2 s (it would be neither realistic nor necessary to update the estimate at each sampling time). For the Gauss–Newton algorithm, ϵ is chosen to be 0.01. The initial guesses used for the parameters are: $\hat{v}_0(0) = 1$ cm s^{-1}, $(\hat{x}_s(0), \hat{y}_s(0)) = (0.5, 1.5)$ cm, $\hat{A}(0) = 0.18$ cm. Since the function f_1 is independent of the traveling velocity v_0, one cannot estimate v_0 directly when $\beta = 0$; in that case, we have approximated the traveling velocity by dividing the difference between the estimated values of x_s at two consecutive estimation instants with the time interval between those instants:

$$\hat{v}_0 \approx \frac{\hat{x}_s(t_{k+1}) - \hat{x}_s(t_k)}{t_{k+1} - t_k}, \tag{10}$$

where $t_{k+1} - t_k = 0.2$ s as mentioned earlier.

Figures 6(a) and (b) show the actual and estimated source locations and the tracking error, respectively, for the two choices of β. The tracking error is computed as the Euclidean distance between the actual source location and the estimated location at a given time. The maximum tracking errors are 0.044 cm for $\beta = 0$ and 0.0441 cm for $\beta = 0.5$. We have also obtained the averages, $\bar{A}$ and $\bar{v}_0$, of the estimates for the dipole vibration amplitude and traveling velocity, where each average is computed by taking the mean of the estimated values over the simulated time period. $\bar{A}$ is 1.87 mm and 1.86 mm when $\beta = 0$ and $\beta = 0.5$, respectively, both of which are close to the true value of 1.91 mm. The values of $\bar{v}_0$, with the estimates computed with (10), are 1.41 cm s^{-1} for $\beta = 0$ and 1.414 cm s^{-1} for $\beta = 0.5$. For $\beta = 0.5$, direct estimation of v_0 results in a value of 1.46 cm s^{-1} for $\bar{v}_0$, which is slightly closer to the true value of 1.5 cm s^{-1} than the values based on indirect approximation (10).

From the simulations above, we see that exploiting the magnitude of the AC component only ($\beta = 0$) can provide

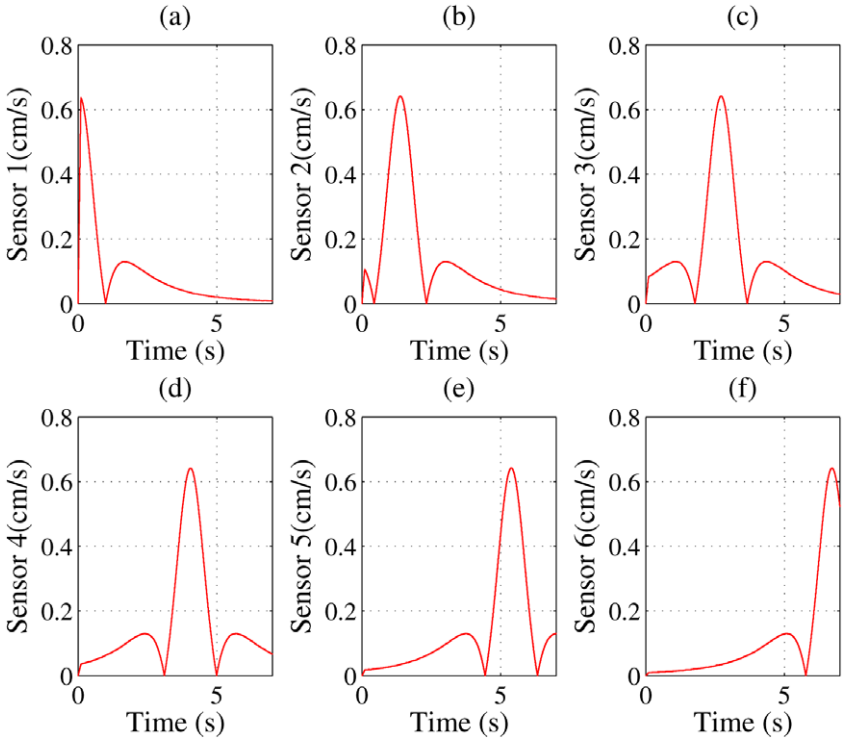

Figure 4. Simulation results: magnitude trajectories of the DC component at the sensor sites.

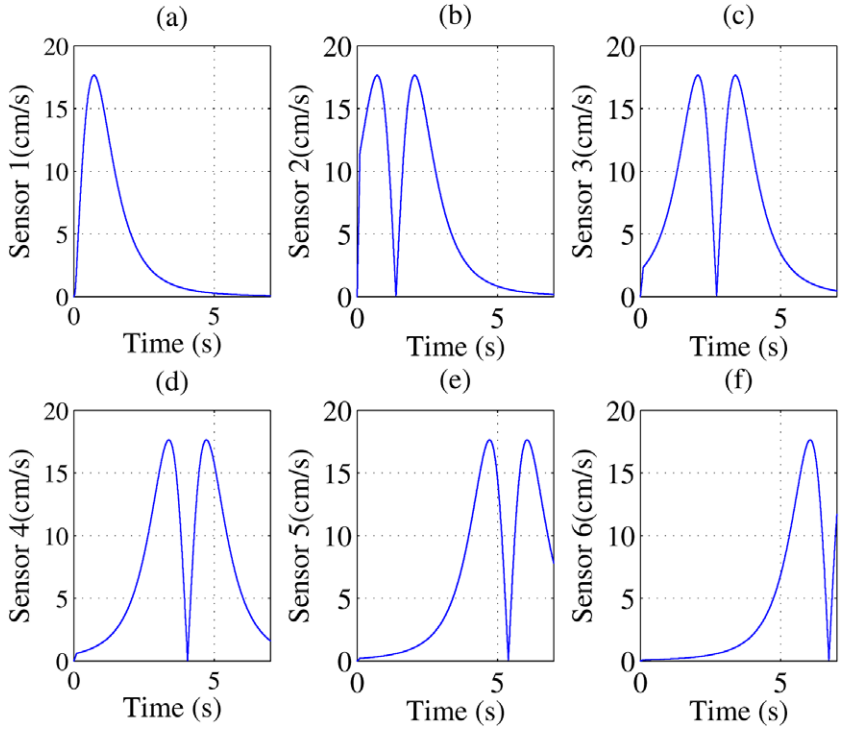

Figure 5. Simulation results: magnitude trajectories of the AC component at the sensor sites.

an estimation performance comparable to that obtained with both DC and AC components ($\beta \neq 0$). There are several advantages in using the AC component only. First, it lowers the computational complexity in the algorithm (7) since one will drop v_0 from the parameter vector θ, which results in a lower-dimension matrix (3×3) to be inverted in each step. Second, in practice the DC component could be subject to significant drift due to sensor characteristics (see section 4) while the AC component is much more robust to noises. Therefore, for the remainder of this paper, we consider $\beta = 0$.

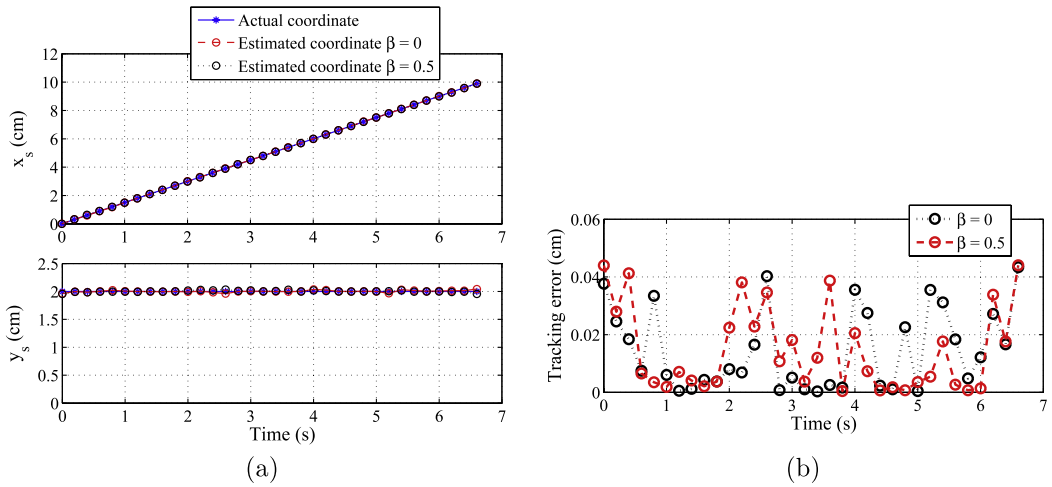

Figure 6. Simulation results on the estimation of the source location: (a) estimated source coordinates; (b) localization error.

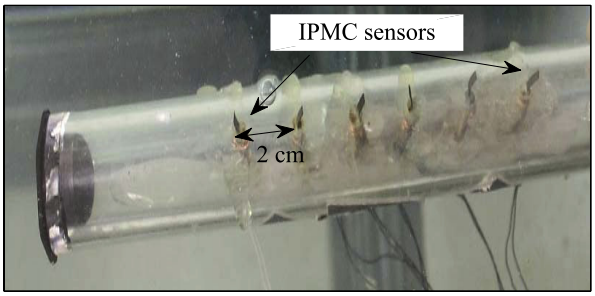

Figure 7. An experimental prototype of an IPMC-based lateral line system.

4. Experimental results

4.1. Experimental setup

We have further validated the proposed localization approach through experiments on an IPMC-based artificial lateral line. The lateral line prototype consisted of six IPMC sensors as shown in figure 7. Each sensor, with dimensions 8 mm × 2 mm × 200 μm, was cut from an IPMC sheet fabricated by the Smart Microsystems Laboratory at Michigan State University, following a recipe similar to the one described in [46]. The sensor-to-sensor separation was 2 cm, resulting in a total span of 10 cm. Each sensor was mounted in such a way that it would bend in the direction parallel to the sensor array, which is denoted as the *x*-direction.

Figure 8(a) shows a schematic diagram of the experimental setup, while figure 8(b) shows a picture of the actual experimental system. The experiments were conducted in a water tank measuring 6 ft long, 2 ft wide and 2 ft deep. A custom-built, DC motor-driven conveyor was used to move a dipole along the *x*-direction in the water. The conveyor track was separated from the lateral line system by 2 cm. The short-circuit current output of each IPMC sensor was amplified with a two-stage amplification circuit [58] before the acquisition (at 20 kHz) and processing by a PC equipped with dSPACE (DS 1104, dSPACE). The dipole source was created with a mini-shaker (model 4810, Brüel and Kjaer, Denmark), the vibration amplitude and frequency of which can be readily controlled through a voltage input to the mini-shaker. A lightweight bar firmly attached to the mini-shaker then translates the vibration to a sphere (aluminum, diameter 1.9 cm) rigidly coupled to the bar. Consistent with the simulation setting, the frequency of vibration used in this work was 40 Hz. The vibration amplitude was 1.91 mm, which was measured with a laser displacement sensor (OADM 20I6441/S14F, Baumer Electric). The dipole source and the IPMC lateral line were completely submerged under water at a depth of about 5 cm. The traveling speed of the dipole was calibrated to be 1.5 cm s^{-1}.

Figure 9 shows the measured instantaneous IPMC short-circuit current from each sensor when the dipole source traveled past the ALL:. Figure 10 shows the DC component of each sensor output obtained through SDFT, with a sliding window of 500 samples (25 ms). It can be seen that the obtained DC component profiles were significantly distorted from the simulated profiles in figure 4. This can be attributed to the difficulty for IPMCs in capturing quasi-static stimuli (since an IPMC sensor responds to *changes* in its mechanical state), which makes the flow measurement at near-DC frequencies susceptible to drifts and noises. Therefore, as justified in section 3, we will instead use the AC components of the IPMC sensor outputs for the dipole tracking.

Figure 11 shows the trajectories of magnitudes of 40 Hz sensor signals obtained via SDFT and expressed in the unit of flow velocity. The conversion from the sensor current amplitude to the flow velocity amplitude is achieved through a sensor calibration procedure. While one could derive a full physics-based model for the IPMC flow sensor by integrating the flow–structure interaction dynamics [66] with the IPMC transduction dynamics [67], this is not necessary if we are only interested in the magnitude gain of the flow sensing dynamics at a given frequency, as in our case here. Instead, we have obtained the magnitude gain as follows. We put the dipole source (40 Hz) at different, fixed locations and collected the outputs of the six sensors accordingly.

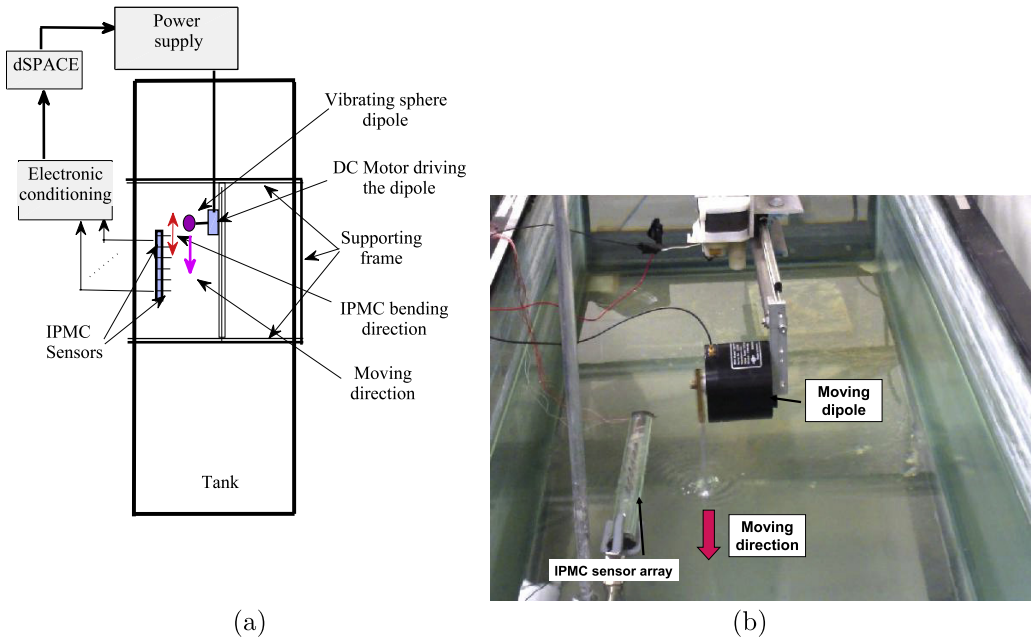

Figure 8. Experimental setup for tracking a traveling dipole source: (a) schematic diagram; (b) picture of the experimental setup.

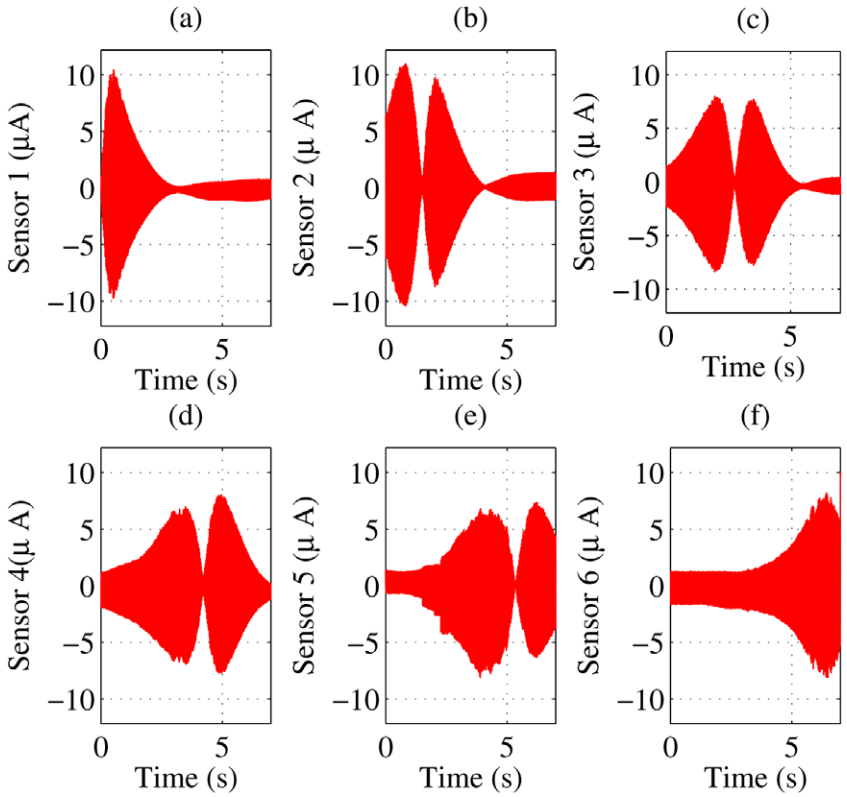

Figure 9. Experimental results: time trajectories of the IPMC sensor output (short-circuit current).

Fast Fourier transform (FFT) was then conducted on the sensor signals to extract their amplitudes at 40 Hz. Next we calculated the theoretical flow velocities (x-component) and thus their amplitudes at each sensor site, for each tested dipole location, based on the potential flow model [60]. Finally, through linear fitting of the measured magnitudes of sensor output to the theoretical flow velocity magnitudes corresponding to different dipole locations, we obtained the calibration gain for each sensor. As can be seen in figure 11, the measured magnitude trajectories at 40 Hz have a similar pattern to that in figure 5, showing a two-peak profile shifting from sensor 1 (left) to sensor 6 (right).

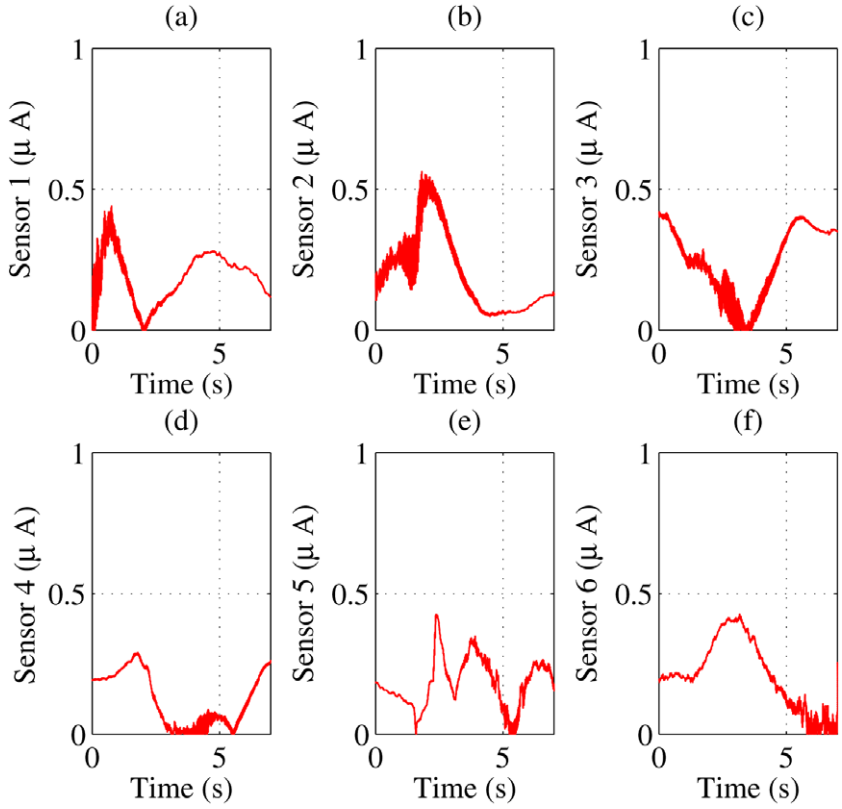

Figure 10. Experimental results: magnitude trajectories of the DC component of the sensor outputs.

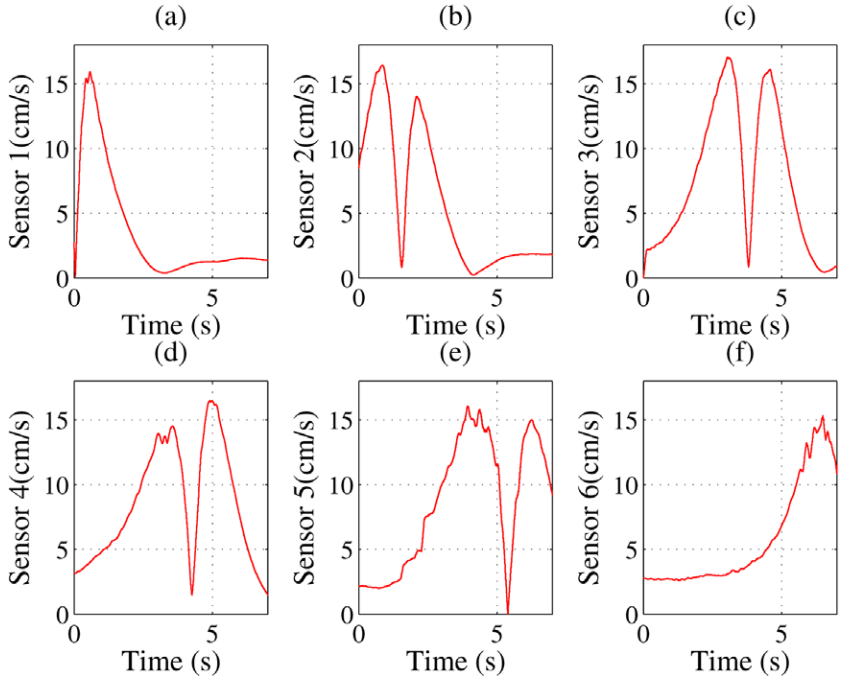

Figure 11. Experimental results: magnitude trajectories of the AC component of the flow velocity at the sensor sites.

Figure 12 shows the actual source locations and the locations estimated based on the magnitude profiles shown in figure 11. Table 1 lists the estimated dipole moving speed and vibration amplitude. The maximum tracking error was 0.33 cm and the errors in estimating v_0 and A were less than 10%, which demonstrates the effectiveness of the proposed estimation approach.

We note that the two peaks in each of figures 11(b)–(e) do not look symmetric to each other. A likely reason is the imperfection of the IPMC sensors; in particular, each sensor

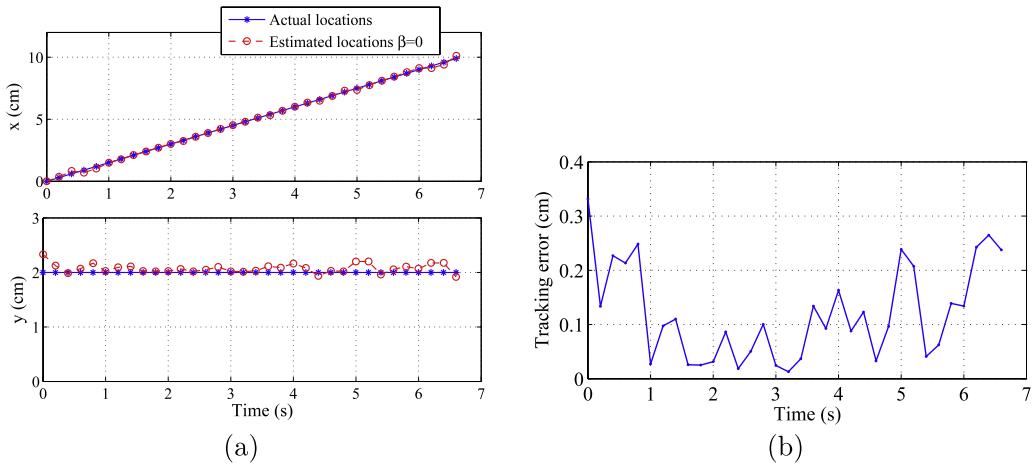

Figure 12. Experimental results for the estimation of the source location: (a) localization, (b) tracking error.

Table 1. Experimental results: estimated velocity (v_0) and vibration amplitude (A).

Parameter	Actual	Estimated	Error
Velocity (cm s^{-1})	1.5	1.4	0.1
Vibrating amplitude (mm)	1.91	2.1	0.19

had slight pre-bending in the absence of flow stimulus, which could result in a slight difference in sensing flows of different directions. While we did not run experiments with the dipole traveling from right to left, we expect comparable overall estimation performance in that case although the estimation error at each physical point could be slightly different.

5. Conclusion

In this paper we investigated an analytical model-based estimation approach to the localization of a moving dipole source using an ALL. The moving speed, vibration amplitude and location of the moving source were assumed to be unknown, and we proposed a Gauss–Newton algorithm to solve the nonlinear estimation problem based on the evolving AC signal magnitudes obtained with SDFT. The effectiveness of the approach was illustrated with simulation and experimental results. In particular, experiments on an IPMC-based ALL prototype have demonstrated that the proposed method is able to simultaneously track the dipole location and estimate its vibration amplitude and traveling speed with small errors. While the paper has focused on a two-dimensional setup, the approach can be readily extended to the three-dimensional setting, where one does not impose constraints on the dipole vibration direction [68] or its traveling direction. We have also assumed that the frequency of the dipole is known; if in practice this is not known *a priori*, one could first run a FFT of the sensor signals to locate potential frequencies of interest. In addition, due to the 'interchangeable' nature of a^3 and dipole velocities in (1), the proposed scheme, with minor modification, can be used to estimate the dipole size a if the vibration amplitude A is known.

Although the dipole vibration frequency was set to be 40 Hz in this work, we note that IPMC sensors can capture vibrations from several Hz [67] to hundreds of Hz [59], which covers well the typical frequency range of a dipole-like stimulus expected in aquatic environments (up to tens of Hz). To maximize the IPMC sensor output, which is closely correlated with the sensor deformation, one needs to properly design the geometry and dimensions of each sensor so that its resonant frequency is close to the expected frequency range of the stimuli.

The estimation performance of the proposed algorithm depends on several factors. First, since the measured flow velocity scales inversely with the cube of the distance between the source and the sensor (see (1)); a larger distance will result in a smaller signal-to-noise ratio (SNR) and thus a larger estimation error. Second, for a given sliding window length (in time), a larger dipole travel velocity v_0 will imply a longer distance traveled and thus a larger variation of actual signal amplitude within that window, which leads to a bigger error in the computed signal amplitude and thus in the estimated dipole location and vibration amplitude. Finally, for a lower dipole vibration frequency, the minimum size of the sliding window, determined by the Nyquist–Shannon sampling theorem, becomes larger; therefore, in order to maintain a given estimation performance, the maximum allowed v_0 will be smaller.

For future work, we are interested in extending the proposed scheme to cases involving multiple traveling dipoles; in particular, the case where multiple dipoles share same vibration frequencies would pose interesting challenges in resolving the locational ambiguity. We also plan to implement the proposed scheme on lateral line prototypes based on microfabricated IPMC sensors [69] with sizes more comparable to biological neuromasts.

Acknowledgment

This research was supported in part by NSF (ECCS 0547131) and ONR (N000140810640, N000141210149).

References

[1] Bleckmann H 1994 Reception of hydrodynamic stimuli in aquatic and semiaquatic animals *Progress in Zoology* ed W Rathmayer (Stuttgart: Gustav Fischer Verlag) pp 1–115

[2] Coombs S 2001 Smart skins: information processing by lateral line flow sensors *Auton. Robots* **11** 255–61

[3] Coombs S, Janssen J and Webb J C 1988 Diversity of lateral lne ystems: evolutionary and functional considerations *Sensory Biology of Aquatic Animals* ed J Atema, R R Fay, A N Popper and W N Tavolga (New York: Springer) pp 553–94

[4] Kroese A B A and Schellart N A M 1992 Velocity- and acceleration-sensitive units in the trunk lateral line of the trout *J. Neurophysiol.* **68** 2212–21

[5] Engelmann J, Hanke W, Mogdans J and Bleckmann H 2000 Hydrodynamic stimuli and the fish lateral line *Nature* **408** 51–2

[6] Hoekstra D and Janssen J 1985 Non-visual feeding behavior of the mottled sculpin, *cottus bairdi*, in Lake Michigan *Environ. Biol. Fishes* **12** 111–7

[7] Pohlmann K, Atema J and Breithaupt T 2004 The importance of the lateral line in nocturnal predation of piscivorous catfish *J. Exp. Biol.* **207** 2971–8

[8] von Campenhausen C, Riess I and Weissert R 1981 Detection of stationary objects by the blind cave fish *anoptichthys jordani* (characidae) *J. Comput. Physiol.* **143** 369–74

[9] Windsor S P, Tan D and Montgomery J C 2008 Swimming kinematics and hydrodynamic imaging in the blind Mexican cave fish (*astyanax fasciatus*) *J. Exp. Biol.* **211** 2950–9

[10] Montgomery J C, Baker C F and Carton A G 1997 The lateral line can mediate rheotaxis in fish *Nature* **389** 960–3

[11] Liao J C 2004 Neuromuscular control of trout swimming in a vortex street: implications for energy economy during the kármán gait *J. Exp. Biol.* **207** 3495–506

[12] Liu C 2007 Micromachined biomimetic artificial haircell sensors *Bioinsp. Biomim.* **2** S162–9

[13] Qualtieri A, Rizzi F, Todaro M, Passaseo A, Cingolani R and Vittorio M D 2011 Stress-driven AlN cantilever-based flow sensor for fish lateral line system *Microelectron. Eng.* **88** 2376–8

[14] Fan Z, Chen J, Zou J, Bullen D, Liu C and Delcomyn F 2002 Design and fabrication of artificial lateral line flow sensors *J. Micromech. Microeng.* **12** 655–61

[15] Yang Y, Chen J, Engel J, Pandya S, Chen N, Tucker C, Coombs S, Jones D L and Liu C 2006 Distant touch hydrodynamic imaging with an artificial lateral line *Proc. Natl Acad. Sci. USA* **103** 18891–5

[16] McConney M E, Chen N, Lu D, Hu H A, Coombs S, Liu C and Tsukruk V V 2009 Biologically inspired design of hydrogel-capped hair sensors for enhanced underwater flow detection *Soft Matter* **5** 292–5

[17] Ozaki Y, Ohyama T, Yasuda T and Shimoyama I 2000 An air flow sensor modeled on wind receptor hairs of insects *Proc. 13th IEEE Int. Conf. on Micro Electro Mechanical Systems (Miyazaki)* pp 531–6

[18] Dijkstra M, van Baar J J, Wiegerink R J, Lammerink T S J, de Boer J H and Krijnen G J M 2005 Artificial sensory hairs based on the flow sensitive receptor hairs of crickets *J. Micromech. Microeng.* **15** S132–8

[19] Klein A and Bleckmann H 2011 Determination of object position, vortex shedding frequency and flow velocity using artificial lateral line canals *Beilstein J. Nanotechnol.* **2** 276–83

[20] Abdulsadda A T and Tan X 2011 Underwater source localization using an IPMC-based artificial lateral line *Proc. 2011 IEEE Int. Conf. on Robotics and Automation (Shanghai)* pp 2719–24

[21] Abdulsadda A T and Tan X 2012 An artificial lateral line system using IPMC sensor arrays *Int. J. Smart Nano Mater.* **3** 226–42

[22] Sarles S A, Pinto P and Leo D J 2011 Hair cell sensing with encapsulated interface bilayers *Proc. Bioinspiration, Biomimetics, and Bioreplication; Proc. SPIE* **7975** 797509

[23] Akanyeti O, Venturelli R, Visentin F, Chambers L, Megill W and Fiorini P 2011 What information do kármán streets offer to flow sensing? *Bioinsp. Biomim.* **6** 036001

[24] Venturelli R, Akanyeti O, Visentin F, Jezov J, Chambers L D, Toming G, Brown J, Kruusmaa M, Megill W M and Fiorini P 2012 Hydrodynamic pressure sensing with an artificial lateral line in steady and unsteady flows *Bioinsp. Biomim.* **7** 036004

[25] Fernandez V I, Maertens A, Yaul F M, Dahl J, Lang J H and Triantafyllou M S 2011 Lateral-line-inspired sensor arrays for navigation and object identification *Mar. Technol. Soc. J.* **45** 130–46

[26] Curcic-Blake B and van Netten S M 2006 Source location encoding in the fish lateral line canal *J. Exp. Biol.* **209** 1548–59

[27] Coombs S and Conley R A 1997 Dipole source localization by mottled sculpin. I. Approach strategies *J. Comput. Physiol.* A **180** 387–99

[28] Pandya S, Yang Y, Jones D L, Engel J and Liu C 2006 Multisensor processing algorithms for underwater dipole localization and tracking using MEMS artificial lateral-line sensors *EURASIP J. Appl. Signal Process.* **2006** 76593

[29] Dagamseh A M K, Lammerink T S J, Kolster M L, Bruinink C M, Wiegerink R J and Krijnen G J M 2010 Dipole-source localization using biomimetic flow-sensor arrays positioned as lateral-line system *Sensors Actuators* A **162** 355–60

[30] Yang Y, Nguyen N, Chen N, Lockwood M, Tucker C, Hu H, Bleckmann H, Liu C and Jones D L 2010 Artificial lateral line with biomimetic neuromasts to emulate fish sensing *Bioinsp. Biomim.* **5** 016001

[31] Franosch J-M P, Sichert A B, Suttner M D and van Hemmen J L 2005 Estimating position and velocity of a submerged moving object by the clawed frog *xenopus* and by fish: a cybernetic approach *Biol. Cybernet.* **93** 231–8

[32] Abdulsadda A T, Zhang F and Tan X 2011 Localization of source with unknown amplitude using IPMC senosr arrays *Proc. Electroactive Polymer Actuators and Devices (EAPAD) XIII; Proc. SPIE* **7976** 797627

[33] Nemat-Nasser S and Li J 2000 Electromechanical response of ionic polymer–metal composites *J. Appl. Phys.* **87** 3321–31

[34] Newbury K M and Leo D J 2003 Linear electromechanical model for ionic polymer transducers—part I: model development *J. Intell. Mater. Syst. Struct.* **14** 333–42

[35] Farinholt K and Leo D 2004 Modeling of electromechanical charge sensing in ionic polymer transducers *Mech. Mater.* **36** 421–33

[36] Akle B J, Bennett M D and Leo D J 2006 High-strain ionomeric–ionic liquid electroactive actuators *Sensors Actuators* A **126** 173–81

[37] Bonomo C, Brunetto P, Fortuna L, Giannone P, Graziani S and Strazzeri S 2008 A tactile sensor for biomedical applications based on IPMCs *IEEE Sensors J.* **8** 1486–93

[38] Chen Z and Tan X 2008 A control-oriented and physics-based model for ionic polymer–metal composite actuators *IEEE/ASME Trans. Mechatron.* **13** 519–29

[39] Chen Z and Tan X 2010 Monolithic fabrication of ionic polymer–metal composite actuators capable of complex deformation *Sensors Actuators* A **157** 246–57

[40] Chen Z, Shatara S and Tan X 2010 Modeling of biomimetic robotic fish propelled by an ionic polymer–metal composite caudal fin *IEEE/ASME Trans. Mechatron.* **15** 448–59

[41] Aureli M, Kopman V and Porfiri M 2010 Free-locomotion of underwater vehicles actuated by ionic polymer metal composites *IEEE/ASME Trans. Mechatron.* **15** 603–14
[42] Pugal D, Jung K, Aabloo A and Kim K J 2010 Ionic polymer–metal composite mechanoelectrical transduction: review and perspectives *Polym. Int.* **59** 279–89
[43] Aureli M, Prince C, Porfiri M and Peterson S D 2010 Energy harvesting from base excitation of ionic polymer metal composites in fluid environments *Smart Mater. Struct.* **19** 015003
[44] Aureli M and Porfiri M 2013 Nonlinear sensing of ionic polymer metal composites *Contin. Mech. Thermodyn.* **25** 273–310
[45] Shahinpoor M and Kim K 2001 Ionic polymer–metal composites: I. Fundamentals *Smart Mater. Struct.* **10** 819–33
[46] Kim K J and Shahinpoor M 2003 Ionic polymer–metal composites: II. Manufaturing techniques *Smart Mater. Struct.* **12** 65–79
[47] Takagi K, Nakabo Y, Luo Z, Mukai T, Yamamura M and Hayakawa Y, An analysis of the increase of bending response in IPMC dynamics given uniform input *EAPAD: Smart Structures and Materials 2006: Electroactive Polymer Actuators and Devices; Proc. SPIE* **6168** 616814
[48] Bonomo C, Fortuna L, Giannone P, Graziani S and Strazzeri S 2006 A model for ionic polymer metal composites as sensors *Smart Mater. Struct.* **15** 749–58
[49] Chen Z, Hedgepeth D R and Tan X 2009 A nonlinear, control-oriented model for ionic polymer–metal composite actuators *Smart Mater. Struct.* **18** 055008
[50] de Gennes P G, Okumura K, Shahinpoor M and Kim K 2000 Mechanoelectric effects in ionic gels *Europhys. Lett.* **50** 513–8
[51] Porfiri M 2008 Charge dynamics in ionic polymer metal composites *J. Appl. Phys.* **104** 104915
[52] Zangrilli U and Weiland L M 2011 Prediction of the ionic polymer transducer sensing of shear loading *Smart Mater. Struct.* **20** 094013
[53] Takagi K, Yamamura M, Luo Z, Onish M, Hirano S, Asaka K and Hayakawa Y 2006 Development of a Rajiform swimming robot using ionic polymer artificial muscles *Proc. 2006 IEEE/RSJ Int. Conf. on Intelligent Robots and Systems (Beijing)* pp 1861–6
[54] Yim W, Lee J and Kim K J 2007 An artificial muscle actuator for biomimetic underwater propulsors *Bioinsp. Biomim.* **2** S31–41
[55] Brunetto P, Fortuna L, Graziani S and Strazzeri S 2008 A model of ionic polymer–metal composite actuators in underwater operations *Smart Mater. Struct.* **17** 025029
[56] Kim K J, Pugal D and Leang K K 2011 A twistable ionic polymer–metal composite artificial muscle for marine applications *Mar. Technol. Soc. J.* **45** 83–98
[57] Tan X 2011 Autonomous robotic fish as mobile sensor platforms: challenges and potential solutions *Mar. Technol. Soc. J.* **45** 31–40
[58] Ganley T, Hung D L, Zhu G and Tan X 2011 Modeling and inverse compensation of temperature-dependent ionic polymer–metal composite sensor dynamics *IEEE/ASME Trans. Mechatron.* **16** 80–9
[59] Chen X, Zhu G, Yang X, Hung D L S and Tan X 2013 Model-based estimation of flow characteristics using an ionic polymer–metal composite beam *IEEE/ASME Trans. Mechatron.* **18** 932–43
[60] Lamb H 1932 *Hydrodynamics* (Cambridge: Cambridge University Press)
[61] Jacobsen E and Lyons R 2003 The sliding dft *IEEE Signal Process. Magn.* **20** 74–80
[62] Shatara S and Tan X 2010 An efficient, time-of-flight-based underwater acoustic ranging system for small robotic fish *IEEE J. Ocean. Eng.* **35** 837–46
[63] Coombs S, Hastings M and Finneran J 1996 Modeling and measuring lateral line excitation patterns to changing dipole source locations *J. Comput. Physiol.* A **178** 359–71
[64] Nguyen N, Jones D L, Yang Y and Liu C 2011 Flow vision for autonomous underwater vehicles via an artificial lateral line *EURASIP J. Adv. Signal Process.* **2011** 806406
[65] Wang J, Alequin-Ramos F and Tan X 2011 Dynamic modeling of robotic fish and its experimental validation *Proc. 2011 IEEE/RSJ Int. Conf. on Intelligent Robots and Systems (San Francisco, CA)* pp 588–94
[66] McHenry M J, Strother J A and van Netten S M 2008 Mechanical filtering by the boundary layer and fluid–structure interaction in the superficial neuromast of the fish lateral line system *J. Comput. Physiol.* A **194** 795–810
[67] Chen Z, Tan X, Will A and Ziel C 2007 A dynamic model for ionic polymer–metal composite sensors *Smart Mater. Struct.* **16** 1477–88
[68] Abdulsadda A T and Tan X 2011 Artificial lateral line-based localization of a dipole source with unknown vibration amplitude and direction *Proc. 15th Int. Conf. on Advanced Robotics (Tallinn)* pp 447–52
[69] Lei H, Li W and Tan X 2012 Microfabrication of IPMC cilia for bio-inspired flow sensing *Electroactive Polymer Actuators and Devices (EAPAD) XIV; Proc. SPIE* **8340** 83401A